

Appendix. Table I: Ship parameters

Description	Parameter	Vaule
Ship length	L_{ship}	103.63m
Vertical length	V_{ship}	82.8m
Ship breadth	B_{ship}	19.2m
Ship draft	H	6m
Ship mass	m	6362.2t
Propeller diameter	D_r	5m
Number of propeller blades	Z	5
Thrust deduction coefficient	t_d	0.2
Rigid body mass matrix and the added matrix	$M + M_A$	Eq.(1)
Hydrodynamic damping matrix	D	Eq.(2)

$$M + M_A = \begin{bmatrix} 6.818 \times 10^6 & 0 & 0 \\ 0 & 7.878 \times 10^6 & -2.596 \times 10^6 \\ 0 & -2.596 \times 10^6 & 3.57 \times 10^9 \end{bmatrix} \quad (1)$$

$$D = \begin{bmatrix} 2.649 \times 10^5 & 0 & 0 \\ 0 & 8.816 \times 10^5 & 0 \\ 0 & 0 & 3.377 \times 10^8 \end{bmatrix} \quad (2)$$

Appendix. Table II: Propeller parameters

Thruster	X(m)	Y(m)	Angle(rad)	Maximum Thrust(KN)
Propeller 1	39.5	0	$\pi/2$	125
Propeller 2	35.3	0	α_2	150
Propeller 3	31.3	0	α_3	150
Propeller 4	-28.5	5	α_4	320
Propeller 5	-28.5	-5	α_5	320

I. DESCRIPTION 1

The constraints of DP system is as follows:

$$s.t. \begin{cases} -U_e^{max} \leq U_e \leq U_e^{max} \\ -\eta_e^{max} \leq \eta_e \leq \eta_e^{max} \\ Kf_{min} \leq Kf \leq Kf_{max} \\ \alpha_{min} \leq \alpha \leq \alpha_{max} \\ \Delta\alpha_{min} \leq \alpha - \alpha_0 \leq \Delta\alpha_{max} \\ B_a(\alpha)Kf = \tau_d - \tau_e \\ P_{min} \leq P_s - P_e \leq P_{max} \\ P_e(k+1) = \min(P_e(k), P_{max} - P_{min}) \end{cases} \quad (3)$$

where, U_e^{max} and η_e^{max} are the maximum deviations of navigation speed and position, respectively; f_{min} and f_{max} are the minimum and maximum thrust, respectively; α_{min} and α_{max} are the minimum and maximum azimuth angle, respectively, and $\Delta\alpha_{min}$ and $\Delta\alpha_{max}$ are their variations, respectively; P_e is a flexible power bias; P_{min} and P_{max} are the minimum and maximum power, respectively. The last term of Appendix. equation (3) is used to ensure enough available power.

The propeller thrust τ and azimuth angles α are obtained through the proposed thrust allocation method, and The propulsion model is formulated by Appendix. equation (4).

$$\begin{cases} Kf = K_T n^2 D_r^4 \rho \\ Q = K_Q n^2 D_r^5 \rho \\ K_T = K_{T1} \left(\frac{V_a}{nD}\right)^2 + K_{T2} \left(\frac{V_a}{nD}\right) + K_{T3} \\ K_Q = K_{Q1} \left(\frac{V_a}{nD}\right)^2 + K_{Q2} \left(\frac{V_a}{nD}\right) + K_{Q3} \end{cases} \quad (4)$$

where K_T and K_Q are the thrust and torque coefficients, respectively; ρ is the density of water; D_r is the diameter of the propeller; V_a is the advance speed of ship; n is the revolution speed of propeller; K_{T1} , K_{T2} , K_{T3} and K_{Q1} , K_{Q2} , K_{Q3} are the thrust parameters and the torque parameters, respectively, which are from the ocean test data.

II. DESCRIPTION 2

$$\begin{cases} J_{ob}(k) = \begin{bmatrix} U_{bat}(k) - OCV(k) + R_p(k)I_p(k) + R_0(k)I_{bat}(k) \\ I_p(k+1) - I_p(k)e^{\frac{-\Delta T}{R_p C_p}} - (1 - e^{\frac{-\Delta T}{R_p C_p}})I_{bat}(k) \end{bmatrix} \\ u_{cr}(k) = \begin{bmatrix} I_p(k) - I_p(k-1) \\ SOC_{bat}(k) - SOC_{bat}(k-1) \\ SOC_{bat}(k) - SOC_{bat}(k-1) \end{bmatrix} \\ Q = \text{diag}[Q_1, Q_2] \\ R = \text{diag}[R_1, R_2, R_3] \end{cases} \quad (5)$$

III. DESCRIPTION 3

Based on the H infinity estimator, equation (19) and equation (20) in the paper can be further formulated by Appendix. equation(6).

$$\begin{cases} x(k) = Fx(k-1) + w(k) \\ y(k) = Hx(k) + v(k) \\ z(k) = L(k)x(k) \end{cases} \quad (6)$$

In this mode, a variance of the error estimation $P = x - \hat{x}$ can be defined, and the operator L and the gain matrix K can be obtained by Appendix. equation(7).

$$\begin{cases} L(k) = (I - Q_L P(k) + H^T V^{-1} H P_k)^{-1} \\ K(k) = F P(k) L(k) H^{-1} V^{-1} \end{cases} \quad (7)$$

where, $I \in R^{3 \times 3}$ is the identity matrix; $Q_L \in R^{3 \times 3}$ and $V \in R$ are the damping factors. On this basis, Appendix. equation(6) can be formulated by Appendix. equation(8).

$$\begin{cases} \hat{x}(k) = Fx(k-1) + K(k-1)(y(k-1) - Hx(k-1)) \\ P(k) = F P(k-1) L(k-1) F^T + W \end{cases} \quad (8)$$

where, $W \in R^{3 \times 3}$ are the damping factors.

IV. DESCRIPTION 4

A iterative model in each cycle is shown in Appendix.equation(9).

$$y(k) = y(k-1) + \varphi(k-1)(C_{bat}(k-1) - C_{bat}(k-2)) \quad (9)$$

Note that the iterative model only involves the terminal voltage of the battery to reduce the influence of unmodeled dynamics, without considering the uncertain internal state variations of the system, thereby the solution of varying pseudo gradient in the discrete time domain can be formulated by Appendix. equation(10).

$$\varphi(k) = \varphi(k-1) + \frac{\eta \Delta u(k-1)}{\mu + |\Delta u(k-1)|^2} (\Delta y(k) - \varphi(k-1) \Delta u(k-1)) \quad (10)$$

where, $\varphi(k) = \varphi(1)$ if the iterative model converges, i.e., $|\varphi(k)| \leq \varepsilon$ or $|\Delta u(k-1)| \leq \varepsilon$ or $sign(\varphi(k)) = sign(\varphi(1))$; ε is a small positive constant, and $\varphi(1)$ is the initial value and $\eta \in (0, 2]$ is a step factor, and μ is a weighting factor used to limit the variations of pseudo gradient.

V. DESCRIPTION 5

The SOC constraint is formulated by Appendix.equation(11).

$$\begin{cases} I_{min}^{char,SOC}(k) = \frac{SOC_{bat}(k) - SOC_{bat}^{max}}{\eta_i \Delta T / C_{bat}(k)} \\ I_{min}^{dis,SOC}(k) = \frac{SOC_{bat}(k) - SOC_{bat}^{min}}{\eta_i \Delta T / C_{bat}(k)} \end{cases} \quad (11)$$

where, $I_{min}^{char,SOC}$ and $I_{min}^{dis,SOC}$ are the minimum and maximum current range of battery based on SOC constraint, respectively; SOC_{bat}^{max} and SOC_{bat}^{min} are the maximum and minimum SOC ranges of battery, respectively.

In the voltage constraint, the voltage boundary to prevent the battery terminal voltage from exceeding the safe voltage range, i.e., the minimum voltage U_{bat}^{min} and the maximum voltage U_{bat}^{max} of battery, shown in Appendix. equation (12).

$$\begin{cases} U_{bat}^{min}(k) = OCV(k) - U_p(k) - R_0(k) I_{max}^{dis,vol}(k) \\ U_{bat}^{max}(k) = OCV(k) - U_p(k) - R_0(k) I_{min}^{char,vol}(k) \\ OCV(k) = [OCV - \frac{\eta_i \Delta T}{C_{bat}} \frac{\partial OCV}{\partial SOC_{bat}} I_{bat}]|_{k-1} \end{cases} \quad (12)$$

where, $I_{min}^{char,vol}$ and $I_{max}^{dis,vol}$ are the minimum pulse current and the maximum pulse current caused by the voltage boundary, shown in Appendix. equation(13).

$$\begin{cases} I_{min}^{char,vol}(k) = \frac{OCV - U_p e^{-\Delta t/\tau} - U_{bat,max}}{\frac{\eta_i \Delta t}{C_{bat}} \frac{\partial OCV}{\partial SOC_{bat}} + R_p(1 - e^{-\Delta t/\tau}) + R_0} \Big|_k \\ I_{max}^{dis,vol}(k) = \frac{OCV - U_p e^{-\Delta t/\tau} - U_{bat,min}}{\frac{\eta_i \Delta t}{C_{bat}} \frac{\partial OCV}{\partial SOC_{bat}} + R_p(1 - e^{-\Delta t/\tau}) + R_0} \Big|_k \end{cases} \quad (13)$$

VI. DESCRIPTION 6

The error augmentation model of HESS is as follows:

$$\begin{cases} x(k+1) = Ax(k) + Bu(k) \\ y(k) = Cx(k) + Du(k) + Eu^2(k) + F \end{cases} \quad (14)$$

A, B, C, D, E are the coefficient matrix, as follows:

$$\begin{cases} A = diag[1, 1, 1, 1] \\ B = diag[-\frac{\eta_{bat}}{3600C_{bat}(k)}, -\frac{\eta_{uc}}{U_{sc}^{oc}C_{sc}}, -\frac{\eta_{bat}}{3600C_{bat}(k)}, -\frac{\eta_{uc}}{U_{sc}^{oc}C_{sc}}] \\ C = diag[0, U_{uc}^{max}(k)I_{uc}(k), 0, U_{uc}^{max}(k)I_{uc}(k)] \\ D = diag[OCV(k), 0, OCV(k), 0] \\ E = diag[-R_0(k), -R_{uc}(k), -R_0(k), -R_{uc}(k)] \\ F = diag[-U_p, 0, -U_p, 0] \end{cases} \quad (15)$$

In the dynamic HESS model, because,

$$\begin{cases} rank([B, AB]) = 4 \\ rank([C, CA]^T) \neq 4 \\ rank([CB, CAB]) = 2 \end{cases} \quad (16)$$

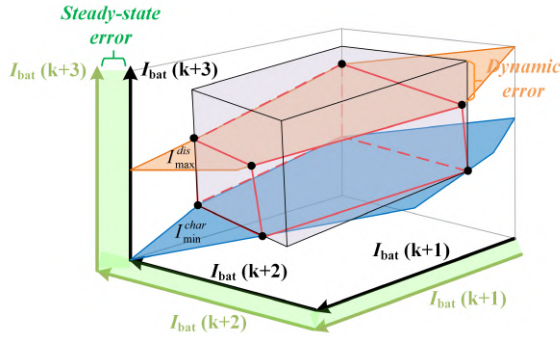
So the system is completely state controllable but not completely observable. For this system, the output variable instead of state variables is required to be controlled. To predict and correct the power error, the PI method as an example can be used to simplify and solve for the current control loop, and the open loop transfer function is shown in Appendix.equation(17).

$$\begin{cases} [\Delta e_{bat}(k), \Delta e_{uc}(k)] = \text{equation(35,36) at } k\text{-th} \\ \Delta I_{bat}(k+1) = (K_{p,b} + \frac{K_{i,b}}{s}) \frac{\Delta e_{bat}(k)}{U_{bat}(k)} \\ \Delta I_{uc}(k+1) = (K_{p,c} + \frac{K_{i,c}}{s}) \frac{\Delta e_{uc}(k)}{U_{sc}(k)} \\ SOC_{bat}(k+1) = SOC_{bat}(k) - \frac{\eta_{bat}}{3600C_{bat}(k)} \underbrace{(I_{bat}(k) + \Delta I_{bat}(k+1))}_{\text{Predictive: } I_{bat}(k+1)} \\ SOC_{uc}(k+1) = SOC_{uc}(k) - \frac{\eta_{uc}}{U_{sc}^{oc}C_{sc}} \underbrace{(I_{uc}(k) + \Delta I_{bat}(k+1))}_{\text{Predictive: } I_{uc}(k+1)} \\ [\Delta e_{bat}(k+1), \Delta e_{uc}(k+1)] = \text{equation(35,36) at } (k+1)\text{-th} \\ \vdots \\ (k + N_L - 1). \end{cases} \quad (17)$$

In the $N_L - th$ prediction interval, the state trajectory and control trajectory of HESS are obtained by Appendix.equation(18).

$$\begin{cases} \begin{bmatrix} SOC_{bat}(k), SOC_{bat}(k+1), \dots, SOC_{bat}(k+N_L-1) \\ SOC_{uc}(k), SOC_{uc}(k+1), \dots, SOC_{uc}(k+N_L-1) \end{bmatrix} \\ \begin{bmatrix} I_{bat}(k), I_{bat}(k+1), \dots, I_{bat}(k+N_L-1) \\ I_{uc}(k), I_{uc}(k+1), \dots, I_{uc}(k+N_L-1) \end{bmatrix} \end{cases} \quad (18)$$

Considering the dynamic SOP range of the battery, an active current constraint of the battery may limit the variations of the above control trajectory, i.e., $[g(I_{bat})|N_{bat}I_{min}^{char} \leq I_{bat} \leq N_{bat}I_{max}^{dis}]$. When $N = 3$, Appendix. Fig. 1 shows the active control constraint of the battery in N dimensions. The internal space of the hexahedron surrounded by red lines is $g(I_{bat}) \leq 0$, and the surface of this hexahedron represents $g(I_{bat}) = 0$. As every two planes of this hexahedron may not be parallel, their gradient may not be in parallel. This brings difficulties in solving the battery dynamic; therefore, the steady-state error and the dynamic error of the battery may be compensated by the ultracapacitor to reduce solution complexity while ensuring power balance.



Appendix. Fig. 1. The active control constraints in three dimensions.

Theorem 1. As the battery operation, If the SOP is constantly changing, so the current constraint / power constraint is active, and the resulted $|\Delta e_{bat}| > 0$. In each control interval, $\Delta e_{bat}(k+1) \neq \Delta e_{bat}(k)$, $(0 < k \leq N_L)$.

Proof. At k -time,

$$\begin{cases} |I_{bat}^{ref}(k)| = |P_{bat}^{ref}(k)/U_{bat}(k)| > |I_{bat}(k)| \\ |\Delta e_{bat}(k)| = |I_{bat}^{ref}(k) - I_{bat}(k)| > 0 \end{cases} \quad (19)$$

where, $i_{bat}^{ref} = \frac{P_{bat}^{ref}}{U_{bat}}$ is the current demand for battery, which from the power decomposition link.

Theorem 2. According to equation (12) in the paper, the state of the HESS system at each moment varies randomly and is bounded along the iteration axis, and the tracking reference trajectory of the system is also non-strict repetitive. In this mode, the control problem of HESS can be converted to a fixed point problem, to ensure the convergence of control problems, a new operator can be obtained: $F = g(x, \dot{x}, u, k) - h(x, k) + u$; where, $g(x, \dot{x}, u, k) = y$ is the function of HESS output, $h(x, k)$ is the reference of HESS output. A control signal u can be solved by the operator within a limited period $[0, T]$ to satisfy: $\{F(u) = u | k \in [0, T], u_k \rightarrow u\}$. At this point,

$$\begin{cases} [g(x, \dot{x}, u, k) - h(x, k)] \rightarrow 0 \\ ||g(x, \dot{x}, u, k) - h(x, k)|| \leq \gamma ||\Delta g(x, \dot{x}, u, k) - h(x, k)|| \end{cases} \quad (20)$$

where, γ is the geometric series.

VII. DESCRIPTION 7

1) *Solution process:* The extreme value of the objective function can obtain the optimal solution: $i_{ILC}(k+1) = i_{ILC} + K_{N-1}[g(k) - h(k)]$. At this point, the iteration relationship of error is as: $[g(k) - h(k)] = L_N[g(k) - h(k)]$; where, K_{N-1} and L_N are the optimal gain matrix and the gradient, they all decrease as N increases.

According to the Karush-Kun-Tucker (KKT) conditions, if the control signal of HESS $u^* = [I_{bat}^d, I_{uc}^d]$ is the minimum, then we can get,

$$\begin{cases} \nabla J(u^*) + \sum_k^N \lambda_j^* \nabla g_j(u^*) = 0, \\ \lambda_j^* \geq 0 \\ \lambda_j^* = 0, j \notin H(u^*) \end{cases} \quad (21)$$

The problem of equation (26) and Appendix.equation (27) in the paper can be written in the following compact form:

$$\begin{cases} \min(\frac{1}{2}\lambda^T H \lambda + \lambda^T P + \frac{1}{2}\gamma^T E^{-1}\gamma) \\ H = ME^{-1}M^T \\ P = \gamma + ME^{-1}F \\ u^* = -E^{-1}(F + M^T \lambda^*) \end{cases} \quad (22)$$

Then, the inequality constrained problem can be transferred to the equality constrained problem to improve the computing efficiency, as follows:

$$\lambda^* = -(M_{act}E^{-1}M^T)^{-1}(\gamma_{act} + M_{act}E^{-1}F) \geq 0 \quad (23)$$

where, M_{act} and γ_{act} are the relative matrix of active constraints. Finally, the quadratic programming procedure method can be used to find the optimal solutions.

2) *Stability analysis of hybrid control system:* The transfer function of the learning algorithm is given as:

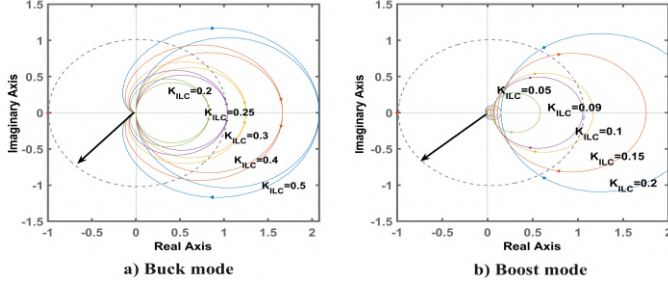
$$G_{ILC}(s) = K_{ILC} \frac{1}{1 + T_c s} \quad (24)$$

where, K_{ILC} and T_c are the gain of the ILC controller and time constant, respectively. When the control interval is $\Delta T = 5e^{-5}s$ with $e = 10$. The proposed control loop $|G_{ILC}(z)CR(z)G_I(z)|$ in the battery and the ultracapacitor are formulated by Appendix. equation(25) and Appendix. equation(26), respectively.

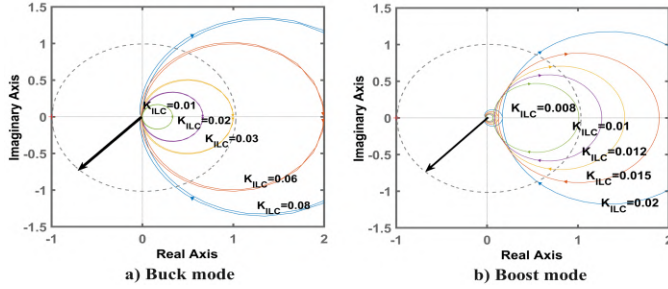
$$\begin{cases} K_{ILC}^{buck} \frac{5.702e^{-8}z^3 + 1.679e^{-7}z^2 - 1.695e^{-7}z - 5.545e^{-8}}{z^4 - 3.946z^3 + 5.837z^2 - 3.837z + 0.9459}, \text{ Buck mode} \\ K_{ILC}^{boost} \frac{1.026e^{-7}z^3 + 3.015e^{-7}z^2 - 3.046e^{-7}z - 9.946e^{-8}}{z^4 - 3.94z^3 + 5.819z^2 - 3.82z + 0.942}, \text{ Boost mode} \end{cases} \quad (25)$$

$$\begin{cases} K_{ILC}^{buck} \frac{2.441e^{-9}z^3 + 7.191e^{-9}z^2 - 7.257e^{-9}z - 2.375e^{-9}}{z^4 - 3.946z^3 + 5.837z^2 - 3.839z + 0.9464}, \text{ Buck mode} \\ K_{ILC}^{boost} \frac{1.844e^{-8}z^3 + 5.42e^{-8}z^2 - 5.476e^{-8}z - 1.788e^{-8}}{z^4 - 3.94z^3 + 5.819z^2 - 3.82z + 0.9402}, \text{ Boost mode} \end{cases} \quad (26)$$

Therefore, the locus of the hybrid control system cannot exceed the unit circle, and the associated Nyquist diagram of the battery and the ultracapacitor are shown in Appendix. Fig. 2 and Appendix. Fig. 3, respectively. To ensure the stability of the system and achieve the fast convergence of the system, the gain K_{ILC}^{buck} and K_{ILC}^{boost} of the battery are chosen as 0.25 and 0.09 by experimentation in buck mode and boost mode, respectively; the gain K_{ILC}^{buck} and K_{ILC}^{boost} of the ultracapacitor are chosen as 0.02 and 0.008 in buck mode and boost mode, respectively.



Appendix. Fig. 2. The locus of $G_{ILC}(z)CR(z)G_I(z)$ of the battery.



Appendix. Fig. 3. The locus of $G_{ILC}(z)CR(z)G_I(z)$ of the ultracapacitor.

VIII. PARAMETERS

Appendix. Table III: Environment simulation parameters

Description	Value	Description	Value
Average wind speed	10 m/s	Ship natural frequency	0.2577
Average wind angle	15 deg	Average current speed	1.2 m/s
Wave height	4 m	Average current angle	30
Wave peak	7 m	Disturbance time constant	1000
Peak wave frequency	0.9 rad/s	Initial position	[0;0;0]

IX. PROPULSION STATE IN DP

Five objective positions for surge, sway, and yaw are set to [20,20,10],[50,50,20],[100,100,30],[150,150,45],[200,200,50]. Within the proposed thrust allocation method considering dynamic storage, the variations in the propulsion states are shown in Appendix.Fig. 4.

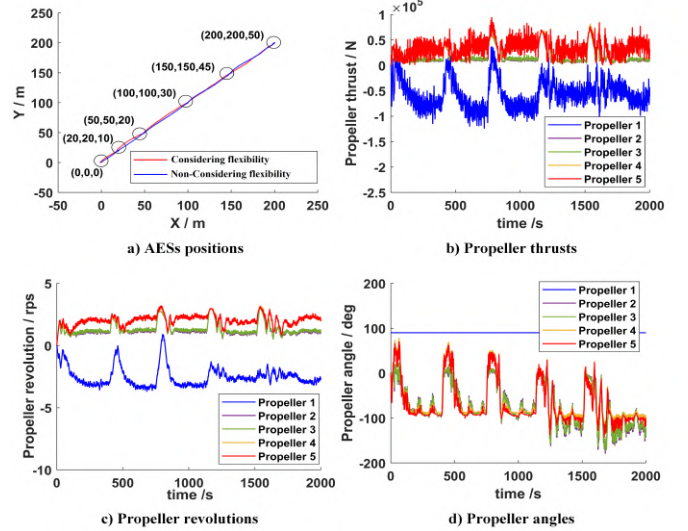
As shown in Fig. 4, the thrust allocation methods can ensure that the ship reaches the designated position, but the thrust,

Appendix. Table IV: The parameters of the tested system

Description	Value	Description	Value
Rated capacity	3350mAh	Standard charging time	4.0hours
Nominal voltage	3.6V	Maximum continuous discharge current	10A
Standard charging current	1.675A	Internal resistance	38mΩ
Charging voltage	4.20±0.03V	Discharging end voltage	2.5V
Current ratio of Battery1 and Battery2	0.5C	Current ratio of Battery3 and Battery4	1C
Current ratio of Battery5 and Battery6	2C	Current ratio of Battery7 and Battery8	3C

Appendix. Table V: Electrical simulation parameters

Description	Parameter	Value
No-load DC voltage	U_{dc}^{ref}	1500V
Initial open circuit voltage of battery	OCV	594 V
Capacity of battery	C_{bat}	1200 Ah
Initial voltage of ultracapacitor	U_{uc}	750 V
Capacity of ultracapacitor	C_{uc}	94.5 F
Maximum current threshold	I_{uc}^{max}	2000A
Minimum current threshold	I_{uc}^{min}	-2000A



Appendix. Fig. 4. The variations in the propulsion states in DP mode.

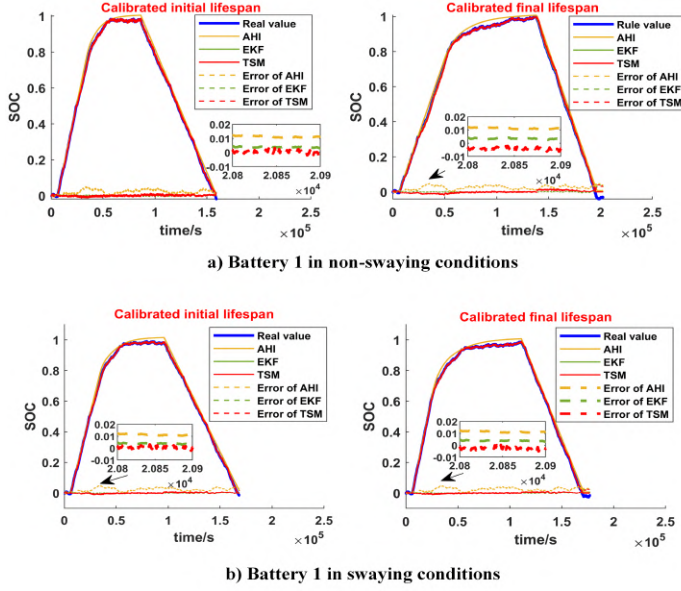
revolution speed, and angle of the propellers vary greatly due to very uncertain environmental disturbances, such as the proposed thrust allocation method in Fig. (b),(c),(d), resulting in drastic variations and unpredictability of the total power demand.

Appendix. Table VI: The state variations of the shipboard main engine

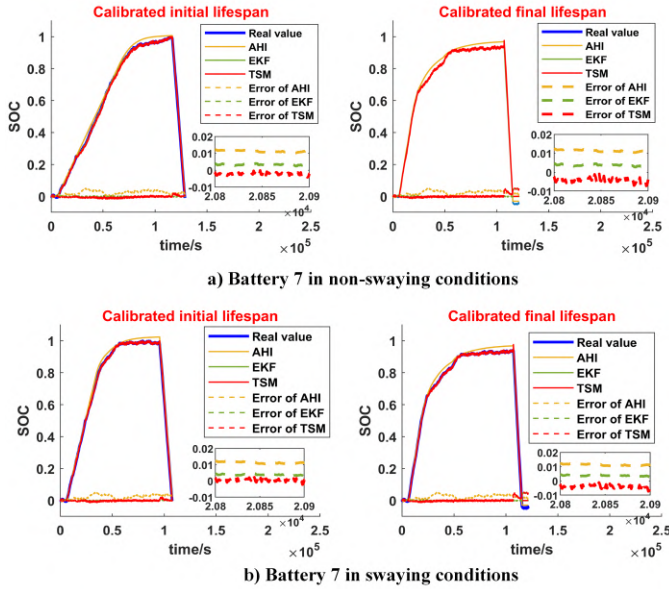
Description	Non-considering flexibility	Considering flexibility
Power fluctuation (kW)	[1558.76, 2842.77]	[1479.92, 2398.32]
Revolution speed (.p.u)	[0.927, 0.969]	[0.94, 0.971]
Frequency (.p.u)	[0.927, 0.968]	[0.94, 0.971]
Voltage (.p.u)	[0.942, 1.019]	[0.957, 0.993]

X. ESTIMATED SOC AND SOH

Under the calibrated initial and final lifetime stages of the battery, The SOC estimation results of battery 1 and battery 7 are shown in Appendix.Fig.5 and Appendix.Fig.6, respectively.



Appendix. Fig. 5. The results of SOC estimation in battery 1.



Appendix. Fig. 6. The results of SOC estimation in battery 7.

The capacity/SOH estimation results are as follows:

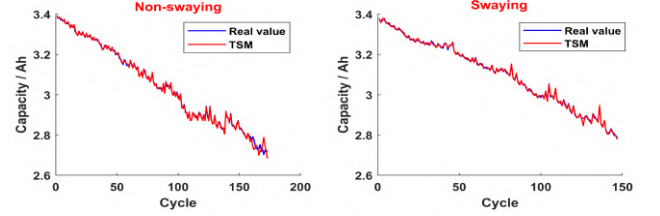
XI. FLEXIBLE OPERATION RANGE

Under different aging conditions, the impact of aging on the feasible power operation range of the battery is shown in Appendix. Fig. 9.

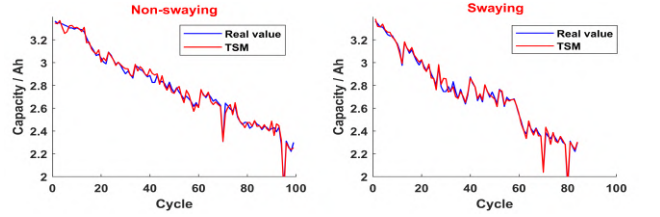
It can be seen from Appendix. Fig. 9 that excessive discharging/charging current ratio not only has a significant impact on the long-term health of the battery, but also has a

Appendix. Table VII: MSE error of SOC estimation

Conditions	Description	AHI	EKF	TSM
Non-swaying	Initial lifespan of battery 1	2.53%	0.59%	0.49%
Non-swaying	Final lifespan of battery 1	2.53%	0.59%	0.49%
Swaying	Initial lifespan of battery 1	2.58%	0.39%	0.22%
Swaying	Final lifespan of battery 1	2.54%	0.53%	0.43%
Non-swaying	Initial lifespan of battery 7	2.58%	1.3%	1.03%
Non-swaying	Final lifespan of battery 7	2.58%	1.3%	1.04%
Swaying	Initial lifespan of battery 7	2.65%	0.19%	0.43%
Swaying	Final lifespan of battery 7	2.58%	1.3%	1.04%



Appendix. Fig. 7. The results of capacity estimation in battery 1.



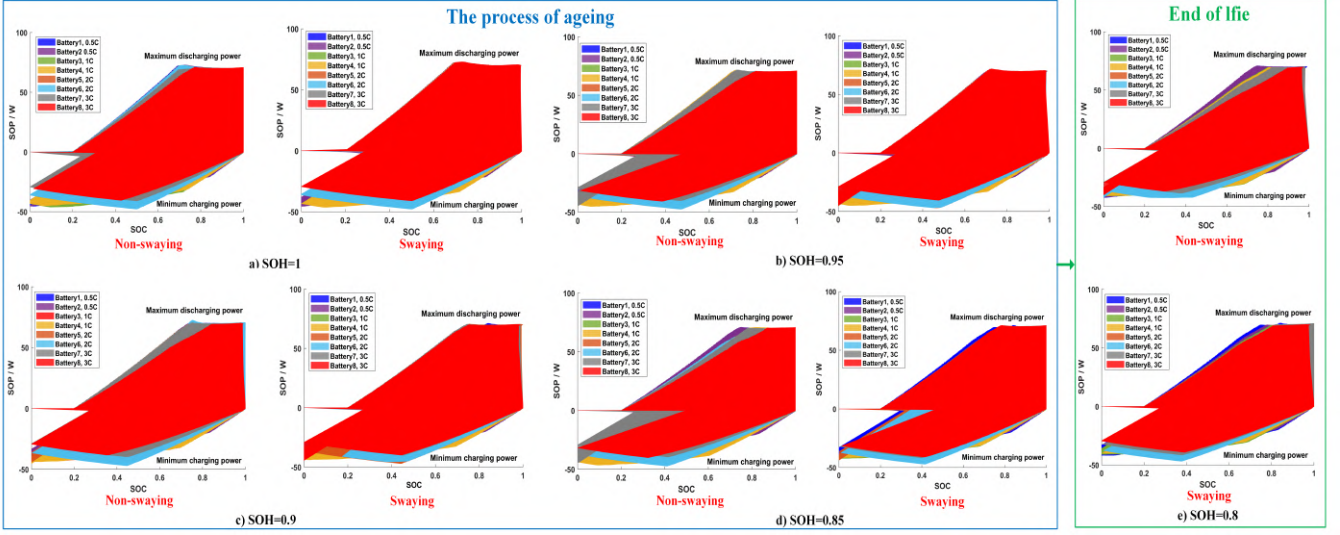
Appendix. Fig. 8. The results of capacity estimation in battery 7.

Appendix. Table VIII: MSE error of capacity estimation

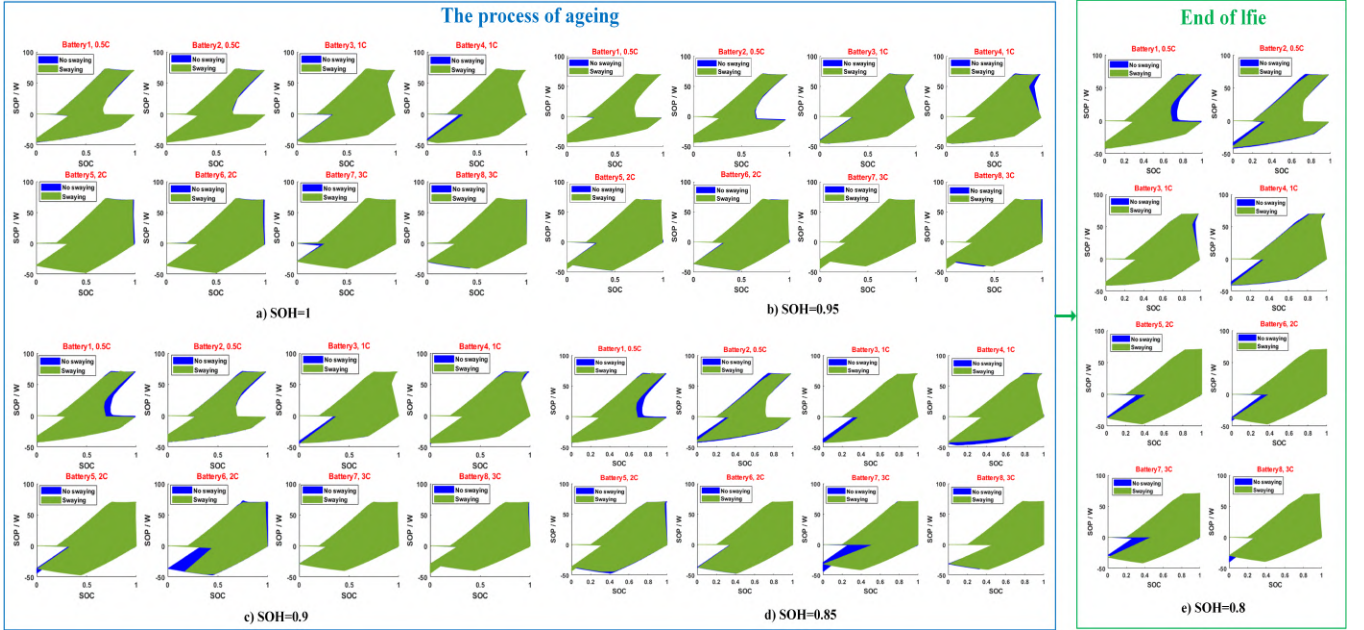
Description	TSM
Battery 1 with non-swaying	0.62%
Battery 1 with swaying	0.6%
Battery 7 with non-swaying	0.36%
Battery 7 with swaying	0.24%

significant impact on the short-term SOP range of the battery. As the current ratio increases, the SOP range will shrink. This situation applies different swaying conditions and different SOHs. Therefore, the variations in the feasible range caused by changes in the current ratio also should be considered in power management.

Under different aging conditions, the impact of ship swaying conditions on the feasible power operation range of the battery is shown in Appendix. Fig. 10. The swaying conditions also have a subtle impact on the short-term SOP range of the battery, and compared with non-swaying conditions, the SOP range is generally smaller in different SOH. This may be the intensification of chemical reactions inside the battery due to swaying conditions, but the mechanism of the internal influence is still unclear, and further impedance spectroscopy experiments are needed to analyze it in future works.



Appendix. Fig. 9. The feasible operation range under different current conditions.



Appendix. Fig. 10. The feasible operation range under different swaying conditions.

XII. POWER CONTROL

In the rigorous dynamic positioning task mode, the state variations in DC bus is shown in Table. IX.

Appendix. Table IX: The variations of DC voltage sags

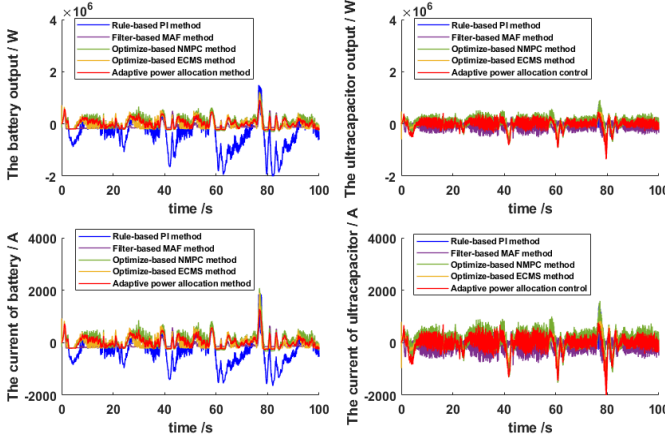
Description	Fluctuation range	Mean value	Standard deviation
Rule-based PI	1352.6V-1535.4V	1497.9V	9.89V
Filter-based MAF	1438.4V-1656.1V	1498V	28.73V
Optimize-based NMPC	1425.9V-1564.8.7V	1497.9V	11.77V
Optimize-based ECMS	1439.8V-1592.2V	1497.9V	17.06V
Adaptive power allocation control	1458V-1574V	1500.5V	7.08V

The variations of the HESS output are shown in Appendix. Fig. 11 and Appendix. Table. X.

Appendix. Table X: HESS output range

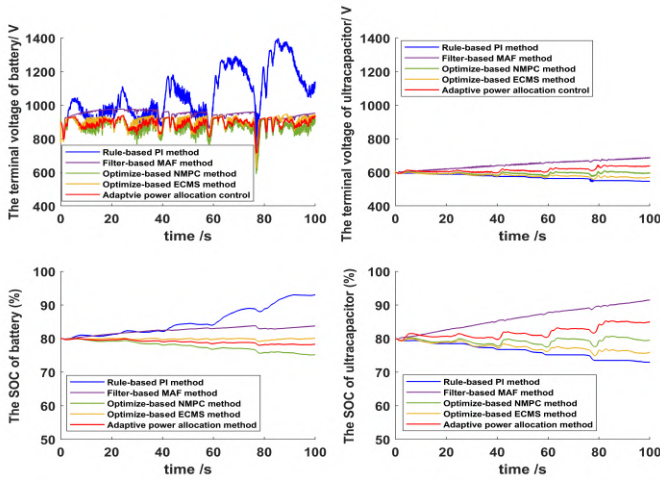
Description	Power range of battery	Power range of ultracapacitor
Rule-based PI	[-2180.8kW, 1488.2kW]	[-150.2kW, 824.3kW]
Filter-based MAF	[-196.4kW, 1162.9kW]	[-559.2kW, 404.2kW]
Optimize-based NMPC	[-292.4kW, 1226.2kW]	[-1063.1kW, 912.8kW]
Optimize-based ECMS	[-211.2kW, 1191kW]	[-738.7kW, 470kW]
Adaptive power allocation control	[-236.4kW, 915.8kW]	[-1355.1kW, 466kW]

Within the proposed method, the battery output is smooth



Appendix. Fig. 11. The variations of HESS output.

and changes between $[-236.4\text{kW}, 915.8\text{kW}]$, due to the accuracy SOP range limitation, thereby the battery does not have to undertake excessive pulse loads, but the ultracapacitor will, which can effectively prevent over-discharging/over-charging of the battery. Then, the state variations of HESS are shown in Appendix. Fig. 12.



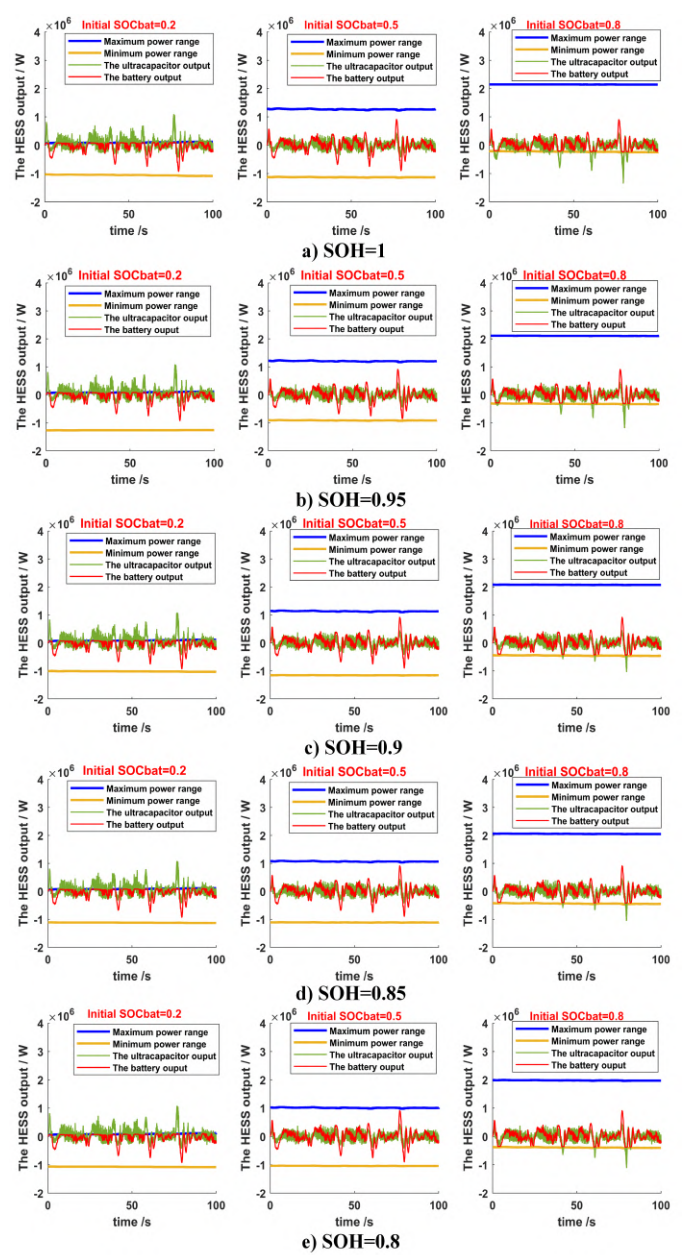
Appendix. Fig. 12. The state variations of HESS.

From Appendix. Fig. 12, when using the rule-based PI method, the unreasonable power profiles may cause drastic voltage changes in the battery due to the fixed power control threshold, which will damage its health. On the premise of ensuring the completion of dynamic positioning tasks, the proposed adaptive power allocation method can adaptively decompose irregular power demand to ensure the voltage and SOC changes of the battery are more stable.

XIII. COUPLING MODEL AT DIFFERENT SCENARIOS

The power variations of HESS in different scenarios are shown in Appendix. Fig. 13, Appendix. Table. XI and Appendix. Table. XII.

The variations of DC voltage at different scenarios are shown in Appendix. Fig. 14 and Appendix. Tabl. XIII.



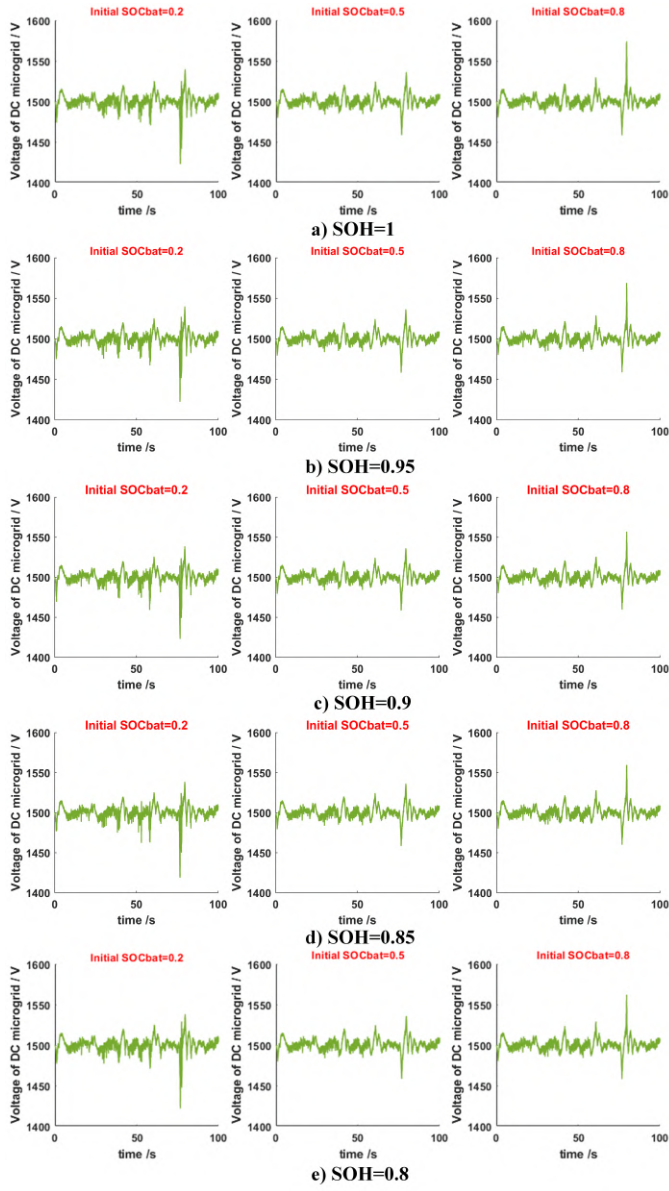
Appendix. Fig. 13. The variations of the HESS power at different SOH.

Appendix. Table XI: The power range of the battery

SOH	Scenario 1	Scenario 2	Scenario 3
1	$[-937.5\text{kW}, 116\text{kW}]$	$[-909.4\text{kW}, 925.9\text{kW}]$	$[-236.4\text{kW}, 915.8\text{kW}]$
0.95	$[-936.3\text{kW}, 112.3\text{kW}]$	$[-851.9\text{kW}, 925.8\text{kW}]$	$[-314.3\text{kW}, 924.4\text{kW}]$
0.9	$[-936.6\text{kW}, 109.1\text{kW}]$	$[-909.4\text{kW}, 925.8\text{kW}]$	$[-439\text{kW}, 927.3\text{kW}]$
0.85	$[-938.5\text{kW}, 106.3\text{kW}]$	$[-909.4\text{kW}, 925.8\text{kW}]$	$[-426.8\text{kW}, 924.1\text{kW}]$
0.8	$[-936\text{kW}, 108.4\text{kW}]$	$[-912.7\text{kW}, 920.6\text{kW}]$	$[-381.9\text{kW}, 926.1\text{kW}]$

Appendix. Table XII: The power range of the ultracapacitor

SOH	Scenario 1	Scenario 2	Scenario 3
1	$[-437.4\text{kW}, 1089\text{kW}]$	$[-431.4\text{kW}, 458.8\text{kW}]$	$[-1355.1\text{kW}, 466\text{kW}]$
0.95	$[-419.4\text{kW}, 1087.4\text{kW}]$	$[-452.5\text{kW}, 458.8\text{kW}]$	$[-1190.7\text{kW}, 475\text{kW}]$
0.9	$[-436.8\text{kW}, 1079.6\text{kW}]$	$[-431.5\text{kW}, 458.8\text{kW}]$	$[-1038.8\text{kW}, 457.9\text{kW}]$
0.85	$[-425.9\text{kW}, 1079.2\text{kW}]$	$[-431.5\text{kW}, 458.8\text{kW}]$	$[-1062.6\text{kW}, 487.7\text{kW}]$
0.8	$[-429.9\text{kW}, 1078.9\text{kW}]$	$[-424.8\text{kW}, 458.8\text{kW}]$	$[-1115.9\text{kW}, 520.8\text{kW}]$



Appendix. Fig. 14. The variations of DC voltage at different scenarios.

Appendix. Table XIII: The variations of DC voltage sags at different scenarios

Description	Fluctuation range in scenario 1 (V)	Fluctuation range in scenario 2 (V)	Fluctuation range in scenario 3 (V)	Average of standard deviation (V)
1	[1422.4,1539.7]	[1458.3,1536.1]	[1458.3,1536.1]	7.23
0.95	[1422.3,1539.8]	[1458.3,1536.4]	[1458.6,1568.9]	7.22
0.9	[1423,1538.6]	[1458.3,1536.1]	[1459.6,1557]	7.22
0.85	[1418.7,1538.5]	[1458.3,1536.1]	[1459.9,1559.6]	7.26
0.8	[1421.9,1538.1]	[1458.3,1535.7]	[1457.8,1562.2]	7.19